Structural in Situ Study of the Thermal Behavior of Manganese Dioxide Materials: Toward Selected Electrode Materials for Supercapacitors

Ouassim Ghodbane,*,† Jean-Louis Pascal,‡ Bernard Fraisse,‡ and Frédéric Favier‡

Institut National de Recherche et d'Analyse Physico-Chimique, Laboratoire des Matériaux Utiles, Pôle Technologique de Sidi Thabet, 2020 Sidi Thabet, Tunisie, and Institut Charles Gerhardt Montpellier, UMR 5253 CNRS, Equipe AIME, Université Montpellier II, Place Eugène Bataillon, cc1502, 34095 Montpellier, Cedex 5, France

ABSTRACT The thermal behavior of a series of MnO_2 materials was investigated toward MnO_2 microstructures under inert atmospheres. The byproduct formed during MnO_2 heat treatments from the room temperature to 800 °C were characterized by in situ X-ray diffraction analyses. It was found that annealing spinel and ramsdellite phases caused the formation of MnO_2 pyrolusite at 200 °C, Mn_2O_3, at 400 °C, and then Mn_3O_4 at higher temperatures. In the case of cryptomelane and birnessite phases, the heating process resulted in the formation of $K_{0.51}Mn_{0.93}O_2$ at 600 °C, while Mn_3O_4 was also formed and still present up to 800 °C. Heat-treating Ni-todorokite and OMS-5 up to about 450 °C led to the formation of $NiMn_2O_4$ and Na_xMnO_2, respectively, and again Mn_3O_4 at higher temperatures. All of these structural transformations were correlated to resulting weight losses of MnO_2 powders, measured by thermogravimetric analyses, during the heating process. Cyclic voltammetry measurements were performed in the presence of 0.5 M K_2SO_4 aqueous solution for annealed cryptomelane, $K_{0.51}Mn_{0.93}O_2$, and Mn_3O_4-based electrodes. It was found that MnO_2 cryptomelane is electrochemically stable upon heating. The long-term charge/discharge voltammetric cycling revealed that the specific capacitance of Mn_3O_4-based electrode is significantly improved from 14 $F \cdot g^{-1}$ (after 20 cycles) to 123 $F \cdot g^{-1}$ (after 500 cycles).

KEYWORDS: manganese oxides • thermal stability • X-ray diffraction • specific capacitance

INTRODUCTION

Manganese dioxide minerals are massively encountered as pigments on the globe's surface and in the deep sea (1). They are widely used in several applications including fuel cells (2), ion exchange (3), molecular absorption (4), lithium batteries (5), catalysis, and electrochemical supercapacitors (6, 7). Numerous synthetic routes were explored to prepare complex manganese dioxides and subsequent electrodes (8−11). Small changes in the synthetic parameters can lead to the formation of solids with distinct compositions and structural characteristics, resulting in distinct catalytic, physicochemical, or ionic exchange properties. The oxidation state of manganese in MnO_2 phases lies between 3.6 and 3.8, indicating that it mostly corresponds to Mn(IV) and Mn(III) in a lower extent (12). The negative electric charge of the framework is balanced by solvated alkaline or alkaline-earth cations since the partial reduction of manganese ions is below the +IV state (4, 13, 14). Usually, the type of lattice defects, the cation content, the manganese oxidation state, and the water content vary in the different manganese dioxides and considerably affect their performances (1). We have very recently reported the syntheses, characterizations, and potential application as supercapacitor electrodes of some manganese dioxides (15). The prepared materials are built on MnO_6 octahedra linked at corners and edges to form various structural arrangements. They exhibit great structural complexity, and three main groups of structures have been identified: three-dimensional (3D) tunnels, bidimensional (2D) layers, and one-dimensional (1D) channels of octahedral framework (15). Our study revealed that electrochemical performances of these various MnO_2 allotropes as supercapacitor positive electrode strongly depends on the material structural arrangement: (i) in the 1D series, the largest channel size leads to the greatest capacitance, and (ii) the electrochemical performance increases with the dimensionality of the structure from the 1D to 3D arrangement. We demonstrated that electrochemical performances mainly relate to the ionic conductivity (and, thus, to the material structure) rather than to the developed surface area.

Additionally, the thermal stability is an important factor that greatly influences the application of MnO_2-based electrodes (16). Previous studies reported that annealing MnO_2 composites leads to the formation of new solids with various structures and many potential applications (8, 17−19). For these reasons, it appears still necessary to systematically investigate the thermal behavior of as-synthesized MnO_2 phases (15), dependently on their structural group, and to

* Corresponding author. E-mail: ouassim.ghodbane@inrap.rnrt.tn. Tel.: +216 71 537 666. Fax: +216 71 537 688.
Received for review July 29, 2010 and accepted November 3, 2010
† Pôle Technologique de Sidi Thabet.
‡ Université Montpellier II.
DOI: 10.1021/am100669k

evaluate the electrochemical behavior of derived manganese oxide materials selected on structural criteria.

The aim of this work is to investigate the thermal stability of several manganese dioxide structures including the 3D MnO_2 spinel, 2D MnO_2 birnessite, and MnO_2 pyrolusite, ramsdellite, cryptomelane, Ni-doped todorokite (Ni-todorokite), and octahedral molecular sieves (OMS-5), of the 1D family. The present study is devoted to the characterization of the products appearing throughout thermal decomposition courses of MnO_2 compounds by in situ X-ray diffraction (XRD) measurements and eventually to select, on the basis of structural characteristics of formed byproduct, candidate metal oxides for the chemical makeup of potential supercapacitor electrode materials. Thermogravimetric analysis (TGA) was performed for the whole MnO_2 set and correlated to the XRD results. Finally, specific manganese oxides were selected and tested as positive electrodes for electrochemical supercapacitors. Cyclic voltammetry (CV) experiments were used to determine the specific capacitance of investigated electrodes. To characterize the electrochemical stability, the electrodes were subjected to long-term charge/discharge voltammetric cycling.

EXPERIMENTAL SECTION

All chemical reagents were analytical grade and have been used as purchased without any further purification. The synthesis techniques of MnO_2 phases were already described in a previous publication (15). Briefly, (i) for MnO_2 birnessite, an aqueous solution (A) was prepared by dissolving 0.04 mol of $KMnO_4$ (99%, Aldrich) and 1.2 mol of NaOH (ACS grade, VWR) in 400 mL of water. Afterward, another aqueous solution (B) was prepared by dissolving 0.112 mol of $MnCl_2 \cdot 4H_2O$ (99%, Aldrich) in 400 mL of water. Solution B was added dropwise to solution A with vigorous stirring in an ice bath. The resulting precipitate was statically aged at room temperature for a day and then washed and dried at 90 °C. (ii) MnO_2 cryptomelane powder was prepared from the ignition in air of MnO_2 birnessite at 400 °C for 60 h. (iii) For MnO_2 Ni-todorokite, an aqueous solution was prepared by dissolving 10 mmol of $MnSO_4 \cdot H_2O$ (99%, VWR) in 20 mL of water under vigorous stirring. A 30 mL aliquot of an aqueous solution of 6 M NaOH was added slowly to produce a tan slurry of $Mn(OH)_2$. After stirring for 15 min, a granular mixture containing 7 mmol of $K_2S_2O_8$ (98%, Aldrich) and 1.4 mmol of $NiSO_4 \cdot 6H_2O$ (99.99%, Aldrich) was added slowly over 30 min while stirring was maintained. The resulting slurry of Ni-doped birnessite was filtered and carefully washed. While still moist, the Ni-doped birnessite was slurried in 200 mL of a 1 M solution of $Ni(NO_3)_2 \cdot 6H_2O$ (98%, Merck). The resulting slurry was stirred overnight in order to produce the Ni-doped buserite (Ni-buserite), which was isolated by filtration and carefully washed. Finally, the moist buserite was added to 15 mL of water in a Teflon-lined stainless-steel autoclave and treated hydrothermally at 160 °C for 24 h. The resulting Ni-todorokite was filtered, carefully washed, and freeze-dried. (iv) For MnO_2 pyrolusite, the Na-doped birnessite powder (1 g) was treated with 100 mL of a 1 M LiCl (99%, Merck) aqueous solution for 1 day under stirring, in order to obtain Li-doped birnessite. The ion exchange was repeated three times to ensure complete exchange of all Na^+ from Na-doped birnessite. MnO_2 pyrolusite was obtained by hydrothermal treatment of Li-doped birnessite with an aqueous solution of 0.5 M H_2SO_4 (ACS grade, Aldrich) and 1 M LiCl for 2 days at 150 °C in a Teflon-lined autoclave. (v) For MnO_2 ramsdelite, stoichiometric amounts of $MnSO_4 \cdot H_2O$ and $(NH_4)_2S_2O_8$ (98%, Aldrich) were dissolved in 100 mL of water, mixed together in a Teflon-lined autoclave and treated hydrothermally at 85 °C for 12 h. The precipitate was separated, washed, and dried at 70 °C. (vi) First, as a MnO_2 spinel precursor, $LiMn_2O_4$ was prepared as follows: $LiNO_3$ (99%, Fisher Scientific) and $Mn(NO_3)_2 \cdot 2H_2O$ (ACS grade, Fisher Scientific) (molar ratio 1:2) were dissolved in a mixture of citric acid (ACS grade, Aldrich) and ethylene glycol (ACS grade, Aldrich) (molar ratio 1:4). The solution was heated at 90 °C for 30 min, and the temperature was subsequently increased to 140 °C in order to trigger esterification and remove the ethylene glycol excess. This solution was heated at 180 °C under vacuum, and the experiment was stopped when a pale-brown powder was obtained. The resulting powder was annealed at 250 °C in air, leading to $LiMn_2O_4$. Finally, the spinel phase was synthesized by hydrolyzing $LiMn_2O_4$ in a 0.5 M HCl (ACS grade, Aldrich) aqueous solution for 24 h at ambient temperature. (vii) For MnO_2 OMS-5, the birnessite powder (0.5 g) was autoclaved at 180 °C for 2 days with 100 mL of a 0.1 M NaOH aqueous solution.

The synthesis methods of $K_{0.51}Mn_{0.93}O_2$ and Mn_3O_4 are described below. All aqueous solutions were prepared using deionized water (18 MΩ, ELGALabWater deionized system).

Synthesis of $K_{0.51}Mn_{0.93}O_2$. MnO_2 cryptomelane powder was loaded in a quartz tube and annealed under vacuum using the following steps: the temperature is first increased from 25 to 80 °C at a heating rate of 5 °C/min. Then, the temperature is stabilized at 80 °C for 30 min before a second temperature increase up to 600 °C at a heating rate of 0.5 °C/min. Finally, the temperature is kept constant at 600 °C for 5 h 30 min before uncontrolled cooling down to room temperature. XRD analyses of as-prepared powder confirmed the formation of $K_{0.51}Mn_{0.93}O_2$ and revealed the presence of diffraction peaks assignable to MnO_2 cryptomelane and Mn_3O_4 phases.

Synthesis of Mn_3O_4. MnO_2 ramsdellite powder was introduced in a quartz tube and annealed under vacuum: the temperature was first increased from 25 to 80 °C at a heating rate of 5 °C/min. Then, it was stabilized at 80 °C during 30 min before a second temperature increase up to 800 °C at a heating rate of 0.5 °C/min. Finally, the temperature is kept constant at 800 °C for 5 h 30min before a cooling down to room temperature. XRD analyses of as-prepared powder revealed the presence of a pure Mn_3O_4 phase.

Thermal Analysis and Physical and Electrochemical Characterization. Temperature-controlled in situ XRD measurements were performed using Bragg–Brentano geometry on a θ-2θ Phillips PW1050 goniometric diffractometer, equipped with a high temperature Anton-Paar HTK16 chamber and a back graphite monochromator. A Cu Kα X-ray source was used in a step scan mode at a scan rate of 10 s/step and a step size of 0.04° (2 θ). MnO_2 materials were dispersed in ethanol, deposited on a platinum sheet, and then placed into the chamber under vacuum. Vacuum was preferred to alternative N_2, Ar, or He inert atmospheres since X-ray counting is more efficient under vacuum, leading to an improved signal/noise ratio and a shorter acquisition time. The heat-treatment ramp was done at a rate of 2 °C/min. The temperature was stabilized during 30 min before recording the X-ray diagram for 5 h at constant temperature.

Thermogravimetric analyses (TGA) were performed using a Netzsh ST 409 PC instrument and a Netzch TG 439 thermobalance. Both are controlled through a Netzch Proteus 4.3 software. The analyses were carried out at a heating rate of 0.2 °C/min, the sample being surrounded by a dynamic (50 mL/min) atmosphere of helium gas (Air Liquide, 99.999%). The electrode preparation and the electrochemical characterization were described elsewhere (15). Briefly, the electrodes were composed of 75 wt % MnO_2 powder, 15 wt % acetylene black (Alfa Aesar, 99.9%), and 10 wt % poly(tetrafluoroethylene) (PTFE; Good-Fellow, 6–9 μm) as a binder. After mixing of the components

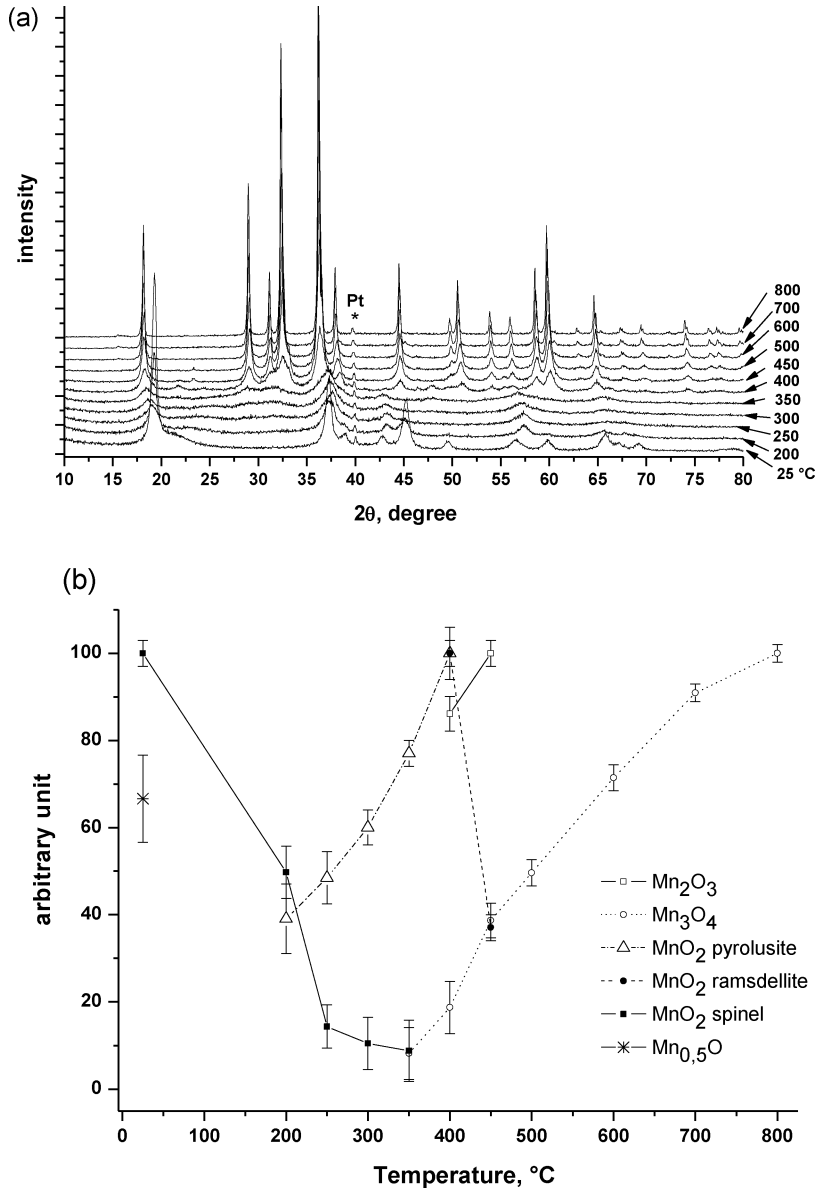

FIGURE 1. (a) In situ XRD patterns of MnO_2 spinel at different temperatures including (111) Pt peak at 39.67° 2θ originates from Pt substrate. (b) Analysis of components formed during the heat treatment of MnO_2 spinel.

in acetone, this slurry was evaporated and the resulting rubberlike paste was roll-pressed into a 200 μm-thick film. Square pieces of film, typically of 2 cm^2 surface area and 30 mg mass, were cut and pressed at 10 tons for 2 min between two stainless-steel grids used as current collectors. Before electrochemical characterization, the electrodes were immersed in the electrolyte solution under vacuum to enhance the electrolyte diffusion into the material bulk.

RESULTS AND DISCUSSION

3D MnO_2 Spinel Phase. In situ XRD measurements of the spinel phase are shown in Figure 1a as a function of the temperature. The pattern of as-synthesized MnO_2 phase (25 °C) depicts signature peaks corresponding to the spinel structure with a few odd reflections assignable to $Li_{0.2}MnO_2$ and $Mn_{0.5}O$ impurities, at 37.2, 42.7, 56.8, and 67.1° 2θ. These peaks disappear when the temperature reaches 200 °C. The heat treatment of MnO_2 spinel leads to a steep decrease of all peak intensities. Main peaks at 39.0, 49.5, 59.7, and 69.2° 2θ disappear when the temperature is increased up to 200 °C. These observations demonstrate the low thermal stability of the 3D structure. On the other hand, new broad peaks appear in the range of 28.8−30° 2θ after annealing the sample up to 250 °C, and their intensities continue to increase between 250 and 400 °C (Figure 1a). These diffraction peaks are related to the 1D pyrolusite phase. The process taking place at about 400 °C results in a migration of lithium out from vacancy sites to form highly crystalline products with more ordered intergrowths, such as 1 × 1 pyrolusite and 2 × 1 ramsdellite tunnels (20). However, the presence of main diffraction peaks assigned to MnO_2 pyrolusite indicates that lithium in the ramsdellite tunnels has only a limited ability to stabilize the ramsdellite lattice against thermal decomposition (11). In fact, pyrolusite is usually known to be the most thermodynamically stable MnO_2 phase. Hackeney and co-workers suggested that a

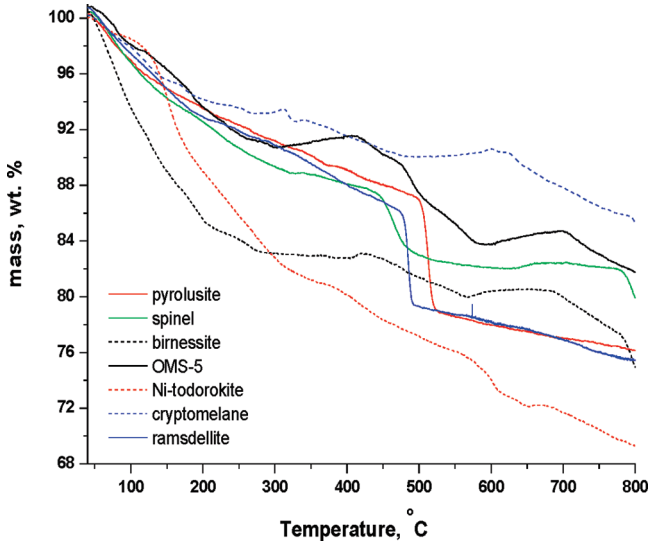

FIGURE 2. Thermogravimetric measurements of as-prepared MnO_2 phases.

single lithium ion is sufficient to stabilize more than 8 MnO_2 units at 350 °C, comparatively to only 4 MnO_2 units at 450 °C (11).

Figure 1b depicts the qualitative analysis of composites formed during the heat treatment of MnO_2 spinel. The XRD patterns exhibited at 350−400 °C gave rise to new diffraction peaks assignable to Mn_2O_3, which is indexed in an orthorhombic system with space group *pbca* and unit cell parameters of $a = 9.4047$ Å, $b = 9.4243$ Å, and $c = 9.4157$ Å. The peak located at 19.2° 2θ shifts to lower 2θ angles during the heat treatment, indicating the reduction of MnO_2 to Mn_3O_4. This component structure is tetragonal with space group $I_{41/amd}$ and cell parameters $a = 5.7574$ Å and $c = 9.4239$ Å. Upon increasing the temperature above 500 °C, the peak width starts to decrease, indicating an increase of crystallinity. Previous studies mentioned that the MnO_2 reduction process involves a multistep mechanism in which MnO_2 is first converted to Mn_2O_3 and subsequently to Mn_3O_4 at higher temperatures (17, 21). In aqueous media, these transformations are accompanied by the oxygen evolution reaction in accordance with the following mechanism (22):

$$4\ MnO_2 \rightarrow 2\ Mn_2O_3 + O_2 \qquad (1)$$

$$6\ Mn_2O_3 \rightarrow 4\ Mn_3O_4 + O_2 \qquad (2)$$

In the present case (under vacuum), peaks assigned to Mn_2O_3 are only detected in a restrained domain of temperature, i.e., between 350 and 400 °C. Annealing the spinel phase up to 400 °C, in our experimental conditions, leads to a mixture of pyrolusite, ramsdellite, and Mn_2O_3. For temperatures higher than 450 °C, only Mn_3O_4 remains.

The weight loss of MnO_2 spinel during heat treatment was investigated by TGA measurements and presented in Figure 2 (green curve). The TG curve depicts multiple weight loss regions. The mass loss of 7.5 wt % up to 200 °C can be attributed to the removal of water. When the temperature exceeds 200 °C, the weight loss slows down until the temperature of 310 °C. In that region, MnO_2 spinel is converted to pyrolusite, as confirmed by XRD data. The gravimetrically stable region located between 310 and 440 °C indicates the completion of the conversion reaction. Previous studies have shown that heating lithiated manganese dioxide up to 350−450 °C leads to the formation of a well-ordered intergrowth structure (11, 23). In the present case, the rapid loss of 4 wt % in the 430−500 °C range coincides with the generation of ramsdellite, Mn_2O_3, and Mn_3O_4 phases. The weight is stabilized beyond 550 °C, where only Mn_3O_4 remains as confirmed by the fingerprint diffraction peaks gained for MnO_2 spinel calcined at 800 °C.

2D MnO_2 Birnessite Phase. Figure 3a focuses on the evolution of XRD patterns of K-birnessite during the heat treatment. The pattern recorded at room temperature under vacuum indicates that (001) and (002) peaks, respectively, located at 12.3 and 24.5°, are shifted to higher 2θ angles at higher temperatures. This behavior indicates a partial dehydration of the interlayer lattice sheets, resulting in a decrease of the interlayer distance from 7.20 to 6.56 Å. Calcination of the birnessite sample gives rise to solids showing higher crystallinities. The lamellar structure collapses around the interlayer cation upon heating, and the structure of the final solid depends on the ionic radius of this cation (24). Figure 3a indicates that diffraction peaks assignable to Mn_3O_4 and $K_{0.51}Mn_{0.93}O_2$ are appearing at 400 and 600 °C, respectively. The 2D layered structure of $K_{0.51}Mn_{0.93}O_2$ crystallizes in orthorhombic system in space group *Cmcm* with unit cell parameters of $a = 2.831$ Å, $b = 5.175$ Å, and $c = 12.66$ Å (25). The structural transformations of MnO_2 birnessite are presented in Figure 3b as a function of the temperature. The formation of Mn_3O_4 (spinel) phase from the birnessite (layered) phase was already reported in the literature (8, 12). On the other hand, $K_{0.51}Mn_{0.93}O_2$ is still thermally stable up to 900 °C and has an interlayer distance of 6.31 Å. It should be noticed that diffraction peaks relative to Mn_2O_3 were not observed upon heating. Such a behavior may be explained by the presence of K^+ ions, between the layers of K-birnessite, that potentially prevent the conversion of MnO_2 to Mn_2O_3 (26).

The TGA curve of MnO_2 birnessite powder is depicted in Figure 2 (dashed black curve). Among all MnO_2 phases in the present series, the curve of K-birnessite powder shows the steepest weight loss up to 200 °C (15 wt %). A similar behavior was reported elsewhere and explained by a larger surface per unit weight covered with H_2O molecules for the birnessite phase (26−28). This important weight loss, corresponding to the desorption/evaporation of H_2O molecules, induces the collapse of the layered structure (28, 29). The water removal from the birnessite lattice is a complex process and generally proceeds in two steps: the first one is the removal of weakly bonded molecules adsorbed on the external surface and uncoordinated interlayer water. The second step corresponds to the loss of water from the hydration shell of interlayer cations (12). When the tempera-

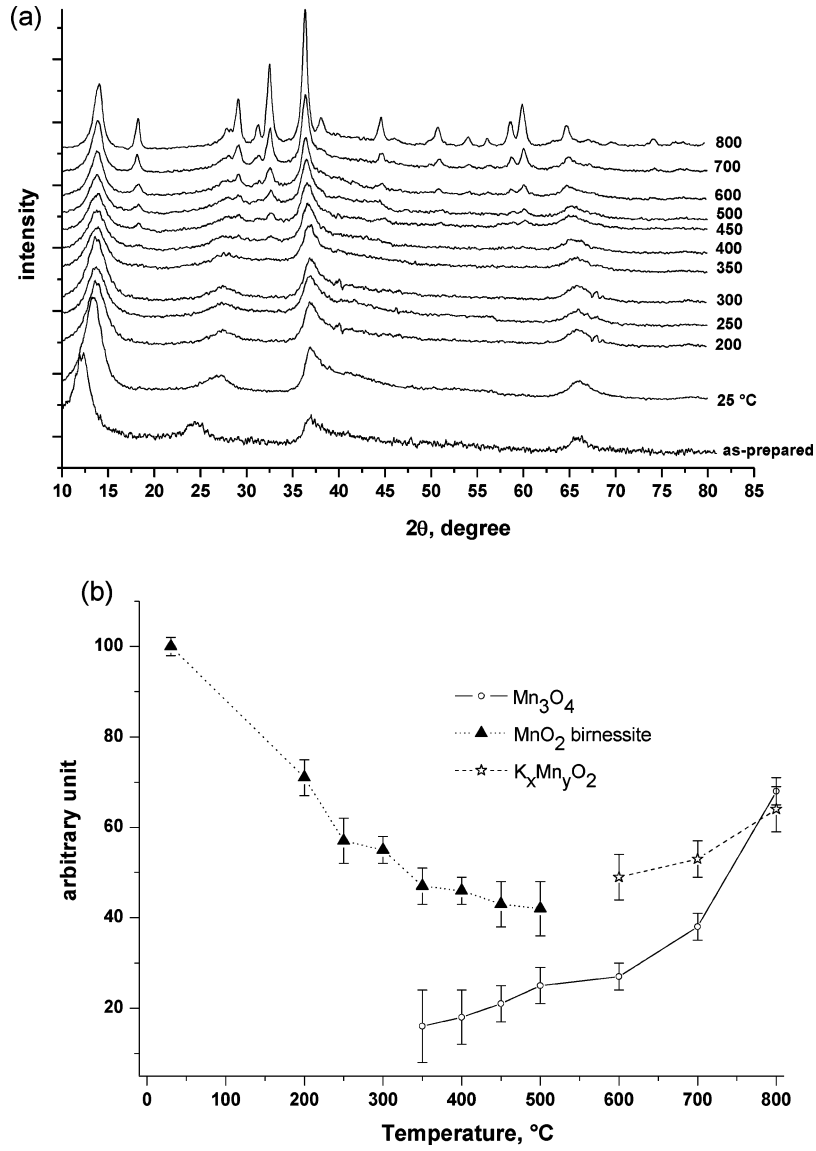

FIGURE 3. (a) In situ XRD patterns of MnO_2 birnessite at different temperatures. (b) Analysis of components formed during the heat treatment of MnO_2 birnessite.

ture exceeds 200 °C, the weight loss rate slows down until roughly stabilizing above 300 °C.

Furthermore, the weight loss of 5 wt % starting at about 420 °C is due to the partial reduction of manganese from tetravalent to trivalent accompanied by oxygen evolution. Another mass loss is observed on the TGA curve following the formation of $K_{0.51}Mn_{0.93}O_2$ at about 700 °C. This is consistent with TGA data of MnO_2 cryptomelane, which show the formation of $K_{0.51}Mn_{0.93}O_2$ at 600 °C (vide infra). Quite surprisingly, there are slight gains in mass observed in the ranges of 404−418 and 567−610 °C. The same behavior was observed under an oxidative atmosphere (oxygen gas) for birnessite powders and nanofibers and was assigned to a subsequent oxidation of Mn^{3+} (10, 31). However, such a weight increase was not observed elsewhere when thermal analyses were performed under an inert dynamic atmosphere (nitrogen gas) (12). In the present case, the gains in mass are attributed to the oxidation of Mn^{3+} to Mn^{4+}, which is probably enhanced by the oxygen released during the conversion of MnO_2 to Mn_3O_4 at lower temperatures. Moreover, the presence of oxygen promotes the formation of $K_{0.51}Mn_{0.93}O_2$ since its manganese oxidation state is higher than in Mn_3O_4.

1D MnO_2 Group. *Pyrolusite (1 × 1 Tunnels).* Chemical and structural changes of MnO_2 pyrolusite upon heating are summarized in Figure 4. The XRD diagram of bare pyrolusite shows the presence of relatively broad peaks, characteristic of a poorly crystalline phase (Figure 4a). As a proof of a good thermal stability for this MnO_2 phase, XRD features remain upon heating up to 400 °C. However, in the temperature range of 25−350 °C, the intensity of peak at 28.84° 2θ relative to (110) planes increases while the corresponding full width at half-maximum (FWHM) decreases, suggesting a progressive crystallization of the phase upon heating. Other diffraction peaks of pyrolusite seem less affected by the thermal treatment with limited changes, if any, in both intensity and FWHM leading to a preferential orientation of the (110) peak characteristic of a crystalliza-

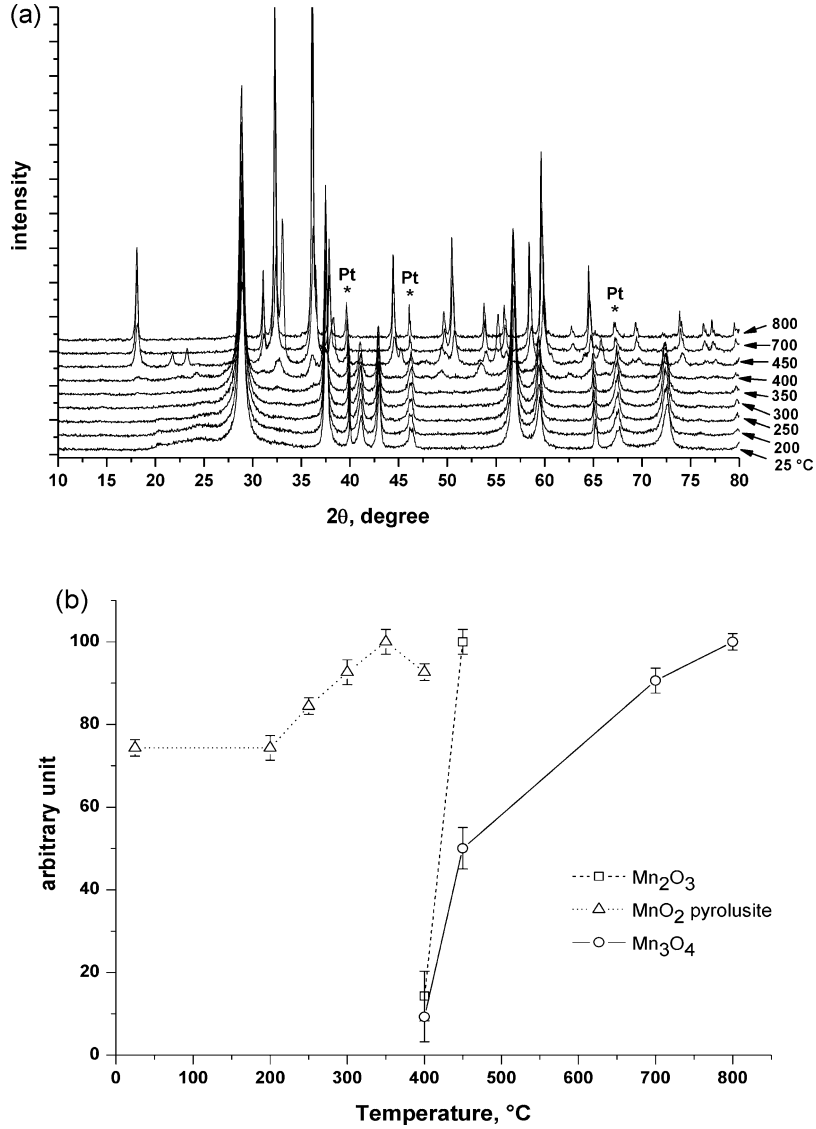

FIGURE 4. (a) In situ XRD patterns of MnO_2 pyrolusite at different temperatures including (111), (200), and (220) Pt peaks at 39.67, 46.28, and 67.30° 2θ, respectively, originate from Pt substrate. (b) Analysis of components formed during the heat treatment of MnO_2 pyrolusite.

tion of the phase in a direction normal to the corresponding planes. At temperatures higher than 400 °C and within a narrow 50 °C range, the shape of the X-ray diagram drastically changes since main peaks related to MnO_2 pyrolusite disappear, suggesting a massive and fast collapse of this phase. On the other hand, new diffraction peaks assignable to Mn_2O_3 and Mn_3O_4 phases are observed at temperature above 450 °C (Figure 4b). The formation of Mn_2O_3 phase from MnO_2 is found to be favored when stabilizing ions, such as K^+ ions, are scarce inside the structure (32). This point is confirmed with MnO_2 pyrolusite since the negligible amount of K^+ ions in the very narrow 1 × 1 tunnels obviously contributes to the conversion of MnO_2 into Mn_2O_3 (32).

TGA curve of pyrolusite, depicted in Figure 2 (red curve), shows a gradual weight loss of 13 wt % in the region of 50−500 °C due to the loss of H_2O molecules, despite the low water concentration in this MnO_2 phase (32). Afterward, the data shows only one thermogravimetric event in the whole temperature range. The sharp weight loss occurring at about 500 °C corresponds to the conversion of MnO_2 pyrolusite to Mn_2O_3 and then to Mn_3O_4. The weight loss nearly stabilizes at temperatures above 550 °C, where only Mn_3O_4 is remaining. All these thermal events are consistent with XRD data.

Ramsdellite (1 × 2 Tunnels). The investigation on the thermal stability of MnO_2 ramsdellite by in situ XRD is shown in Figure 5. It should be noticed that the as-prepared ramsdellite compound includes a pyrolusite phase. In fact, MnO_2 ramsdellite is a random intergrowth of ramsdellite (1 × 2) and pyrolusite (1 × 1) domains that may be described in terms of De Wolff disorder and microtwinning (33). This usually results in a poorly crystalline phase, as indicated by the broad diffraction peaks in the XRD diagram recorded at room temperature (Figure 5a). Upon increasing the temperature, the peak FWHMs tend to decrease, indicating that the structure progressively changes to crystalline. The stability of MnO_2 ramsdellite is usually ensured by the structural water present in tunnels (16). The removal of water during the heat treatment had a significant effect on the tunnel

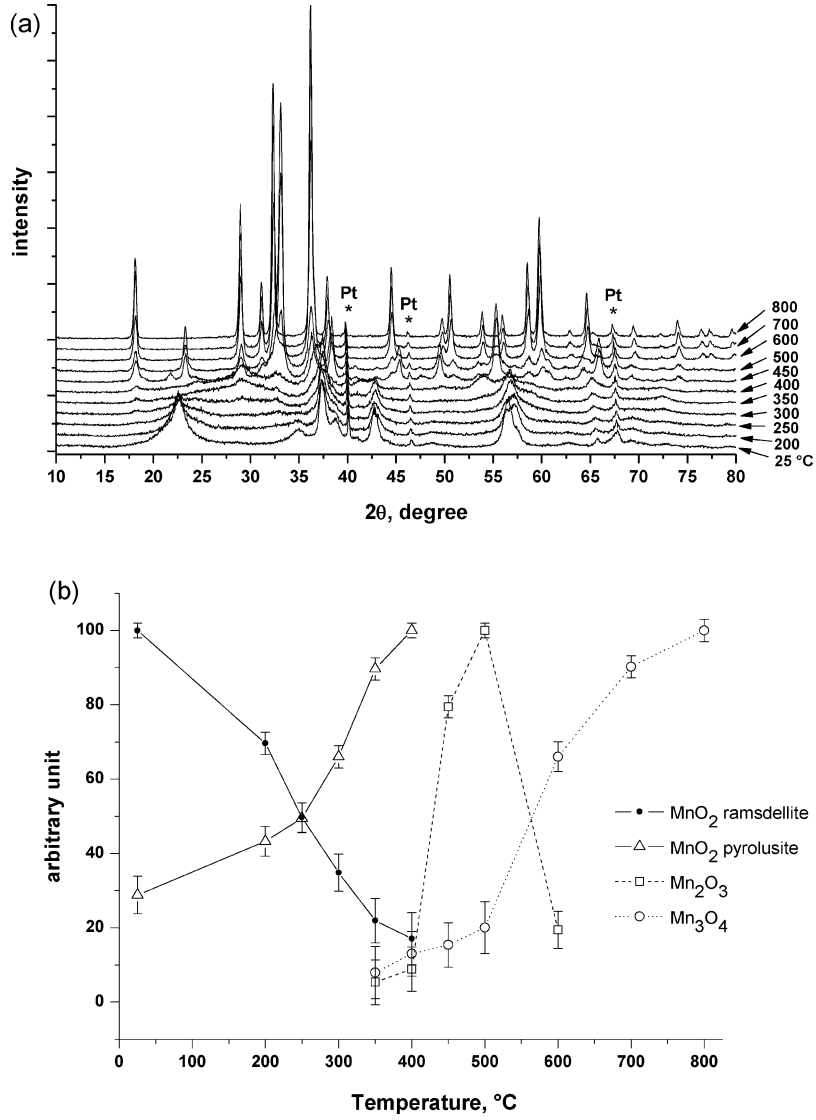

FIGURE 5. (a) In situ XRD patterns of MnO_2 ramsdellite at different temperatures including (111), (200), and (220) Pt peaks at 39.67, 46.28, and 67.30° 2θ, respectively, originate from Pt substrate. (b) Analysis of components formed during the heat treatment of MnO_2 ramsdellite.

structure. When the temperature reaches 400 °C, the peak reflection at 22.5° 2θ disappears completely while the peak intensity at 28° 2θ increases. This indicates a progressive conversion of the ramsdellite into a pyrolusite phase upon heating up to 400 °C (Figure 5b). Consequently, the annealed ramsdellite sample acts as the pyrolusite one. It is shown that increasing the temperature promotes the formation of Mn_2O_3 between 350 and 500 °C and Mn_3O_4 until 800 °C.

The thermogravimetric profile of ramsdellite powder (Figure 2, blue curve) is found to be very similar to the one of pyrolusite (Figure 2, red curve). This behavior is definitively related to the similarity between the enthalpies of formation of these two MnO_2 forms (34) and suggests that the framework stability is moderately influenced by the openness of the structure. Moreover, these similarities are also consistent with a progressive conversion of ramsdellite in pyrolusite. The TGA profile of ramsdellite shows two main weight loss regions in the temperature ranges from room temperature to 400 °C and from 400 to 800 °C. The weight loss of water in the first region shows two parts. The mass loss of 7 wt % in the range 30−200 °C is related to physisorbed water and to water chemically bonded in the tunnels. The mass loss of structural water (7 wt %) between 200 and 400 °C was already ascribed to the dissipation of water (35). According to the XRD data, the conversion of ramsdellite to pyrolusite occurs from 200 to 400 °C. Thus, the mass loss observed in that range could be attributed to this structural transformation. Lv et al. mentioned that, with dissipation of structural water, tunnels in MnO_2 ramsdellite start to collapse and form the pyrolusite phase (16). The thermogravimetric accident occurring at 480 °C is due to the conversion of pyrolusite to Mn_2O_3 accompanied with some oxygen release. As mentioned for MnO_2 pyrolusite, the small weight loss occurring at temperatures above 550 °C is assigned to the reduction reaction of Mn_2O_3 into Mn_3O_4.

Cryptomelane (2 × 2 Tunnels). Figure 6a presents the modification of the X-ray diagram of MnO_2 cryptomelane

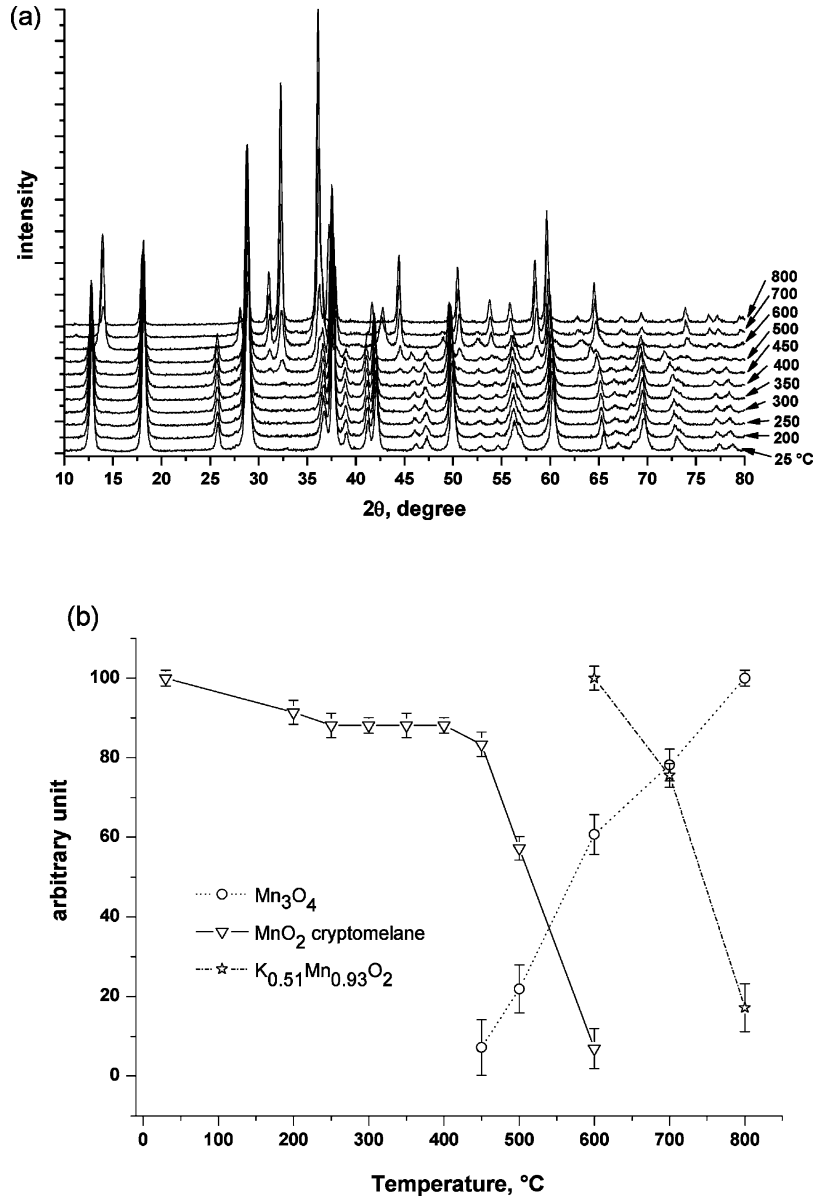

FIGURE 6. (a) In situ XRD patterns of MnO_2 cryptomelane at different temperatures. (b) Analysis of components formed during the heat treatment of MnO_2 cryptomelane.

during heat treatment. This MnO_2 phase shows the highest thermal stability among all MnO_2 phases investigated during this work. In fact, the cryptomelane pattern remains during heat treatment until reaching a temperature of 400 °C. Then, the main diffraction peaks significantly decrease or shift when the sample was annealed up to 600 °C, leading to the degradation of the crystal structure and the formation of new components as depicted in Figure 6b. It is shown that diffraction peaks related to Mn_3O_4 appear from 450 °C and remain at 800 °C, while Mn_2O_3 corresponding peaks are not observed. These observations contrast with those reported by DeGuzman et al. when heating reactions were performed under oxygen atmosphere (8). They demonstrated that oxygen stabilizes the intermediate Mn_2O_3 phase and delays the conversion temperature from Mn_2O_3 to Mn_3O_4. However, under inert atmosphere, oxygen evolution is too limited to participate in MnO_2 to Mn_2O_3 conversion (8). For that reason, Mn_2O_3 could not be detected in the present experimental conditions. The XRD pattern recorded at 600 °C indicates the appearance of a new diffraction peak at 13.96° 2θ indexed to (002) planes of $K_{0.51}Mn_{0.93}O_2$. The conversion process from 1D to 2D arrangement occurs by losing the channel pillars, allowing to the structure to compress and to transform to a layered 2D organization.

The thermal profile of cryptomelane powder, presented in Figure 2 (dashed blue curve), shows the smallest weight loss (about 10 wt %) in the temperature range between room temperature and 350 °C. This is due to the high thermal stability of this phase and to the small amount of water present in its structure since the cryptomelane was synthesized via a thermal route at 450 °C for 60 h (15). It was recently suggested by Valente et al. that the weight loss caused by heating cryptomelane powders under nitrogen atmosphere up to 400 °C is mainly associated with the removal of molecules adsorbed at the material surface such as H_2O and CO_2 (36). These molecules are successively

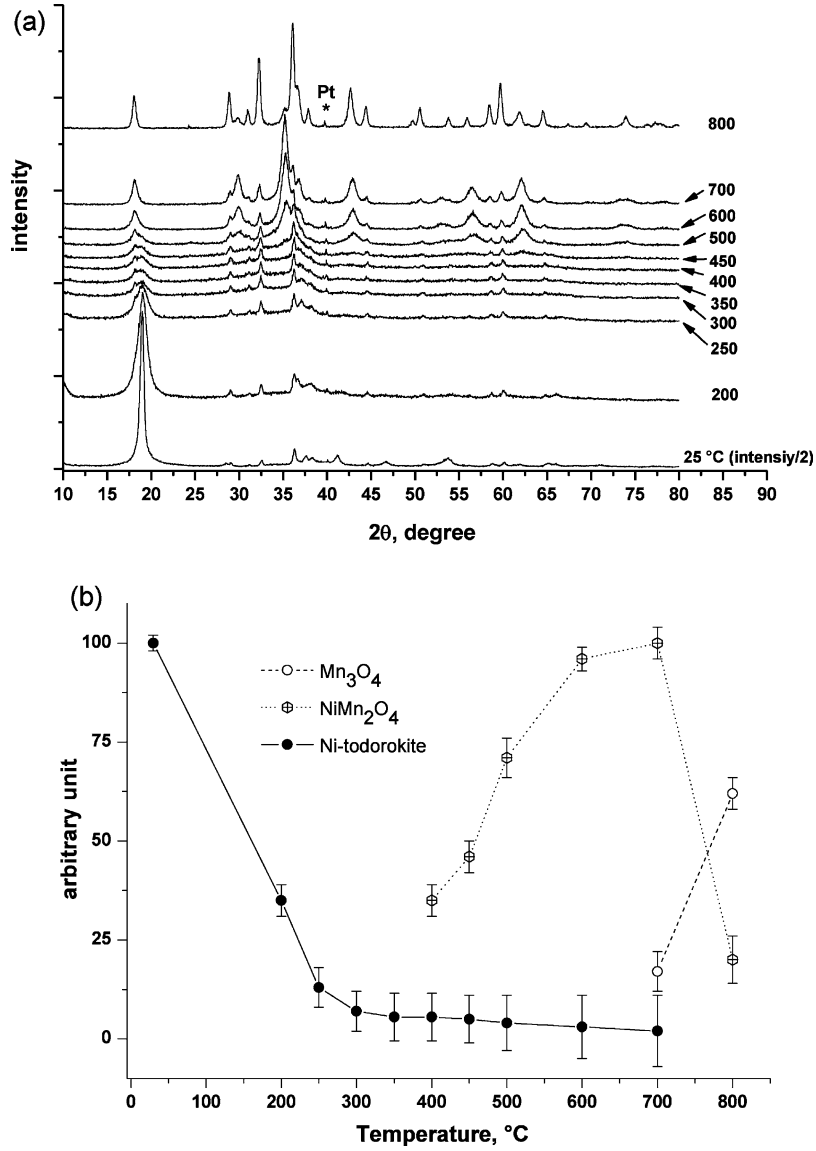

FIGURE 7. (a) In situ XRD patterns of MnO_2 Ni-todorokite at different temperatures including (111) Pt peak at 39.67° 2θ originates from Pt substrate. (b) Analysis of components formed during the heat treatment of MnO_2 Ni-todorokite.

desorbed according to their interaction strengths with the cryptomelane surface. Generally, the release of water molecules occurs below 100 °C, and then, carbon dioxide is removed at higher temperatures (36). Previous studies performed in the presence of oxygen revealed that heating MnO_2 cryptomelane leads to the release of many components including H_2O, CO_2, and hydrogen−carbonate species ($-HCO_3$) (37). Figure 2 shows a stabilization of the thermal curve between 450 and 600 °C. The latter temperature coincides with the conversion of MnO_2 cryptomelane to $K_{0.51}Mn_{0.93}O_2$ and Mn_3O_4, as revealed by XRD. Increasing the temperature over 600 °C results in a mass loss of 5 wt %, assigned to the degradation of $K_{0.51}Mn_{0.93}O_2$ phase.

Ni-Todorokite (3 × 3 Tunnels). XRD diagrams of heat-treated Ni-todorokite are depicted in Figure 7a. They show that the main peak located at 18.9° 2θ, relative to (102) planes, is obviously attenuated by heating up to 250 °C. This demonstrates the rapid degradation of the 3 × 3 channel structure upon the loss of water, which ties the Ni cation by H bonding to oxygen atoms of MnO_6 octahedron building the channel walls (15). The breakdown reactions of todorokite are also due to its significant structural disorder (38). It is shown that, above 400 °C, Ni-todorokite started to transform while new broad peaks, attributed to spinel $NiMn_2O_4$ phase, appear between 30 and 40° 2θ (Figure 7b). The crystal structure of $NiMn_2O_4$ presents a 3D arrangement and was indexed to a tetragonal system (space group $I_{41/amd}$, cell parameters of $a = 5.9764$ and $c = 8.4201$) (39). On the other hand, some Ni-todorokite remained at this stage of heat treatment and even up to 700 °C. XRD measurements demonstrate that $NiMn_2O_4$ remains stable during the heat treatment up to 700 °C, in agreement with previous studies on decomposition residues of Ni-todorokite at very high temperatures (~800 °C) (21). Products appearing throughout thermal decomposition courses of cation-doped todorokites gave rise to XRD patterns depending on the type of the divalent metal ion included (21, 40). For example, in the presence of Mg or Co, diffraction peaks obtained at 500 °C

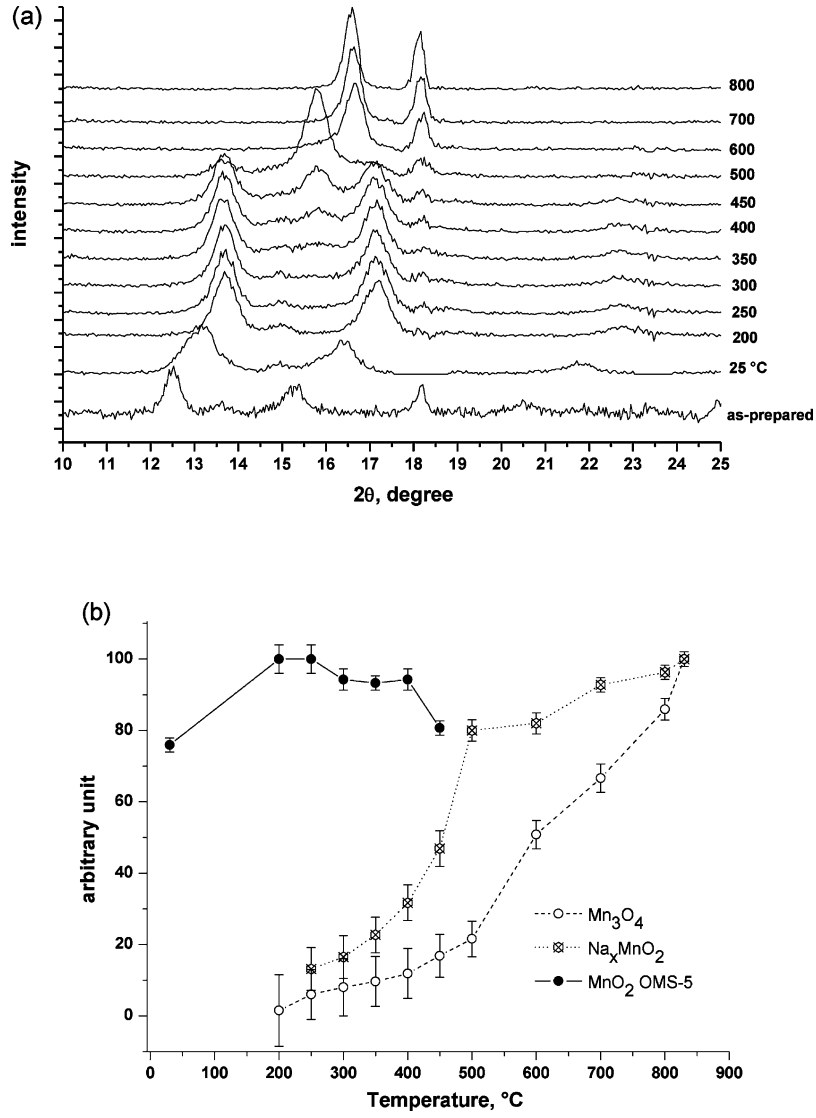

FIGURE 8. (a) In situ XRD patterns of MnO_2 OMS-5 at different temperatures. (b) Analysis of components formed during the heat treatment of MnO_2 OMS-5.

are characteristic of the formation $MgMn_2O_4$ or $CoMn_2O_4$, respectively (40). In the present case, the formation of Mn_3O_4 is found to occur at about 700 °C and displays strong characteristic peaks when the temperature reaches 800 °C. Since the present experiment was carried out under vacuum, the break down temperature has shifted compared to what was observed under air. It is noteworthy that the remaining (102) planes shifts to lower 2θ values, but the corresponding peak never completely disappears even at the maximum temperature of 800 °C. This remain suggests the presence of a Ni-based phase that formed along with Mn_3O_4 at higher temperatures, in order to accommodate Ni cations originally present in the todorokite phase.

Figure 2 (dashed red curved) shows that, among all MnO_2 phases investigated here, Ni-todorokite undergoes the most important weight loss (30 wt %) upon heating up to 800 °C, confirming its very low thermal stability. The large weight loss of 18 wt % up to 315 °C should be due to the loss of both adsorbed and coordinated water molecules in the large 3 × 3 tunnels of Ni-todorokite (41). The weight loss of about 5 wt % in the range of 400−580 °C is assigned to the departure of water and the dehydroxylation of the material surface, together with the conversion of Ni-todorokite in $NiMn_2O_4$. In the temperature range of 700−800 °C, the weight loss of about 7 wt % is attributed to the reduction of Mn_2O_3 into Mn_3O_4 and its related compounds. A detailed mechanism of the todorokite to Mn_3O_4 transformation was already described by Post et al. (38). They suggested that the reduction of Mn and the release of oxygen result first in the breakdown of the octahedral framework and, then, in the release of H_2O molecules. In the present case, the opposite phenomena takes place since the loss of structural water occurs at lower temperature than the transformation of the todorokite structure. For this reason, it is more plausible to assume that water loss from todorokite tunnels leads the framework to collapse.

Na OMS-5 (2 × 4 Tunnels). To the best of our knowledge, the investigation of the thermal behavior of OMS-5 phase is presented for the first time hereafter. The structure of OMS-5 is characterized by a complex X-ray diagram due to its low symmetry, large parameters, and

preferential crystallites orientation (15). For these reasons, the XRD thermal investigation of OMS-5 is investigated between 10 and 25° 2θ range (Figure 8a) in order to simplify the diagram interpretation. The choice of that 2θ domain is appropriate since it corresponds to the diffraction peaks relative to OMS-5 as well as to all components formed during the heat treatment. Figure 8a shows that the (200) peak shifts from 12.40 to 13.18° 2θ just by introducing the sample in the Anton-Paar vacuum chamber. This behavior reflects a crushing of the channels with a decrease of the distance from 7.13 to 6.71 Å (a/2) due to the partial dehydration of the 4 × 2 channel. Annealing the sample up to 200 °C results in an extra shift of the (200) peak to 13.69° 2θ (a/2 = 6.69 Å). These results indicate that OMS-5 behaves like the birnessite powder in that temperature range. Moreover, the diagram of the sample heat-treated up to 500 °C shows a collapse of the (200) planes and the appearance of a strong peak at 15.8° 2θ, indicating the degradation of OMS-5 structure to the profit of new 2D layered phases. The structural transition from 1D tunnels to 2D layers implies the removal of channel pillars, formed by two MnO_6 octahedral building blocks. This mechanism allows the channel-structure to collapse. The byproduct formed during the heat treatment of OMS-5 is summarized in Figure 8b. Regarding the 2D derived phases, diffraction peaks assignable to Na_xMnO_2 are obtained. The structure of these layered compounds is quite similar to that reported in the literature for $Na_{0.52}MnO_2$ and $Na_{0.51}Mn_{0.93}O_2$ (42). $Na_{0.52}MnO_2$ is indexed to an orthorhombic type with space group *Cmcm* and cell parameters of $a = 2.834$ Å, $b = 5.216$ Å, and $c = 11.28$ Å. $Na_{0.51}Mn_{0.93}O_2$ crystallizes in a hexagonal system with space group *P63/m* and cell parameters of $a = 2.866$ Å and $b = 11.165$ Å. The interlayer distance of Na_xMnO_2 varies from 5.72 Å (temperature range of 200−500 °C) to 5.43 Å (temperature range of 500−900 °C). Among the derived components, Mn_3O_4 was also identified from 250 °C and still thermally stable up to 800 °C.

The thermal decomposition course of OMS-5 is shown to be multistep (Figure 2, black curve). TGA curve shows a weight loss of 10 wt % upon heating up about 300 °C, followed by a slight increase of 1 wt % up to 410 °C. This weight loss is only attributed to the departure of water from the large 2 × 4 tunnels. XRD measurements of the heat-treated sample indicated that OMS-5 structure is roughly decomposed to a layered component (Na_xMnO_2) from 300 °C. This transformation may be related to the small weight gain observed between 300 and 410 °C. Similarly, the increase of temperature from 600 to 700 °C results in another weight gain of 1 wt % that might be assigned to further structural transformations of Na_xMnO_2. According to XRD data, it is suggested that weight losses of 8 wt % (at 510−590 °C) and 3 wt % (at 700−800 °C) are mainly due to the progressive dehydration of Na_xMnO_2 layers and to the reduction of manganese leading to the formation of Mn_3O_4.

The whole set of byproduct obtained by heat-treating the prepared MnO_2 phases and their corresponding reactions pathways are summarized in Figure 9. Annealing any MnO_2 form investigated here leads to Mn_3O_4 as a final product. Only ramsdellite, spinel, and pyrolusite phases generate Mn_2O_3 as an intermediate product during their heat treatments. Other products may also be obtained following different heat treatments; they present either a 3D arrangement, such as $NiMn_2O_4$, or 2D structures, such as Na_yMnO_2 and $K_{0.51}Mn_{0.93}O_2$.

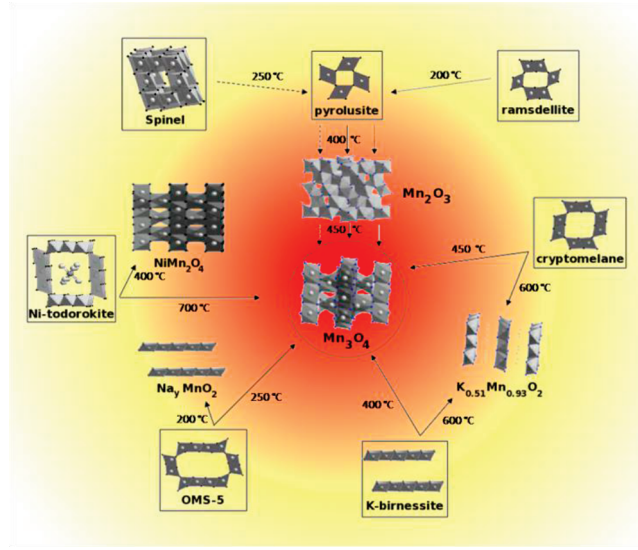

FIGURE 9. Structural modifications of as-prepared MnO_2 phases (boxed) during heat treatments. Mn_3O_4 is the common final product. Dotted and dashed arrows present the reaction pathways of MnO_2 ramsdellite and spinel, respectively. Transition temperatures are indicated on the figure.

Electrochemical Investigations. Hydrous manganese dioxides have shown pseudocapacitive behavior in aqueous electrolytes containing alkali cations and were extensively studied as positive electrode materials for supercapacitors. Very recently, it has been demonstrated that the 3D microstructure of MnO_2 spinel and the 2D layer-structure of the birnessite phase show the best electrochemical performances among a large variety of MnO_2 compounds (15). For the 1D channel group, i.e., pyrolusite, ramsdellite, cryptomelane, and OMS-5 series, it was concluded that the specific capacitance may be improved by increasing the channel size (15). Taking into account these observations and structure-performance relationship, specific byproducts derived from MnO_2 heat treatments are selected and tested as alternative electrode materials for supercapacitors. Among the manganese oxides investigated here, Mn_3O_4 and $K_{0.51}Mn_{0.93}O_2$ are expected to generate potentially attractive electrochemical performances due to their 3D spinel and 2D layered structures, respectively. $K_{0.51}Mn_{0.93}O_2$ may be obtained by annealing MnO_2 cryptomelane up to 600 °C, as depicted in Figure 6b, despite the fact that such preparation route leads to $K_{0.51}Mn_{0.93}O_2$ mixed with Mn_3O_4 and MnO_2 cryptomelane. The synthetic methods of $K_{0.51}Mn_{0.93}O_2$ and Mn_3O_4 are detailed in the Experimental Section. On the other hand, XRD results indicate that the crystal structure of MnO_2 cryptomelane is still stable after annealing up to 400 °C (Figure 6b). Because of this remarkable thermal stability, it appeared worth investigating the electrochemical behavior of MnO_2 cryptomelane heat-treated up to 400 °C following

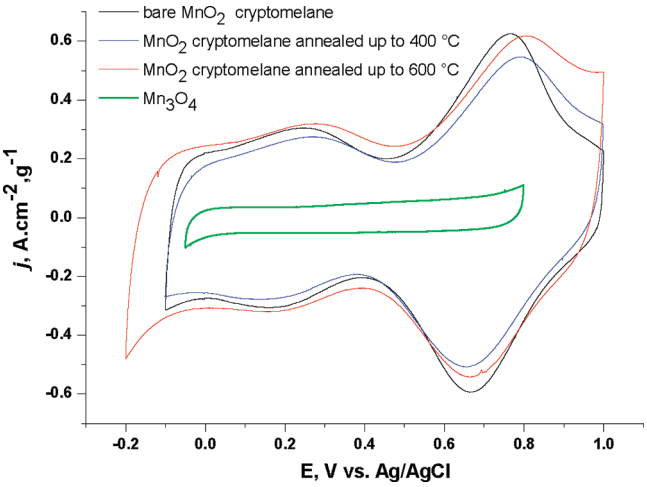

FIGURE 10. CV curves (fifth cycle) of Mn_3O_4 and bare and annealed MnO_2 cryptomelane-based electrodes recorded in aqueous 0.5 M K_2SO_4 at 5 mV · s^{-1}.

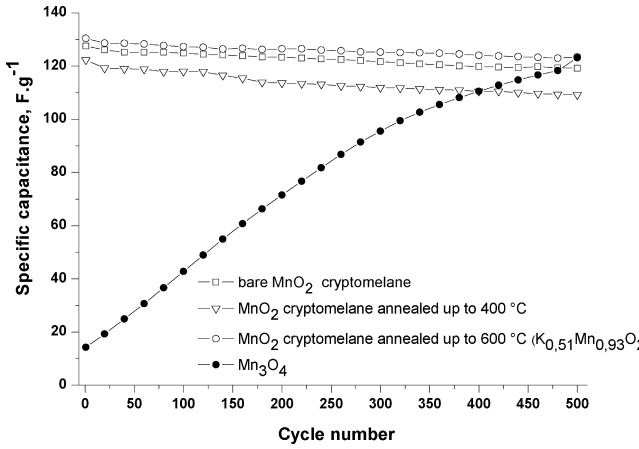

FIGURE 11. Variation of the specific capacitance during 500 cycles for Mn_3O_4 and bare and annealed MnO_2 cryptomelane-based electrodes. The specific capacitance is estimated from the CV curves recorded in 0.5 M K_2SO_4 at 5 mV · s^{-1}.

the same experimental conditions, in order to compare it to that of the bare cryptomelane.

The CV curves of manganese oxides composite electrodes are depicted in Figure 10. Measurements were done in an aqueous 0.5 M K_2SO_4 electrolyte within different potential window ranges. It should be noted that CV curves presented in Figure 10 correspond to the fifth recorded cycle, i.e., after stabilization of the electrode response to cycling. For MnO_2 cryptomelane, the shape of CV curves is invariable after heat treatments up to 400 and 600 °C. Therefore, MnO_2 cryptomelane is electrochemically stable upon thermal treatments. The two redox waves present on CV curves of bare and heat-treated cryptomelane were already attributed to an insertion/extraction mechanism of K^+ cations into the material bulk (15). Generated $K_{0.51}Mn_{0.93}O_2$ electrochemically behaves just like pristine MnO_2 cryptomelane. Measured capacitance of cryptomalane thermally treated at 600 °C is just a few F/g greater than that of the bare cryptomelane. The transition temperature from MnO_2 cryptomelane to $K_{0.51}Mn_{0.93}O_2$ is quite narrow, and both phases are obtained as a mixture together with Mn_3O_4 traces. Despite these "impurities", a greater capacitance difference was expected compared to bare cryptomelane thanks to the presence of the $K_{0.51}Mn_{0.93}O_2$ 2D phase with an anticipated improved performance level. On the other hand, a typical rectangular shape of pseudocapacitive behaviors is obtained for the Mn_3O_4-based electrode. This electrode however exhibits the lowest current densities and the smallest potential window (43). The specific capacitance values were measured for heat-treated cryptomelane and Mn_3O_4 phases over extended charge−discharge voltammetric cycling. The resulting values are plotted in Figure 11 as a function of the cycle number. A significant improvement of the capacitance of Mn_3O_4 occurs by extended cycling. Mn_3O_4 demonstrated a very low capacitance value (14 $F.g^{-1}$) after 20 cycles and reached its maximum value (123 $F.g^{-1}$) after 500 cycles. Previous studies described Mn_3O_4 to be transformed into Mn_2O_3 and then MnO_2 phases during the potential cycling (44, 45). The structure of Mn_3O_4 may be transformed into hydrated manganese (di)oxide by electro-oxidation during the charge/discharge process, which results in improved capacitance values (44, 46). Further studies on these phenomena are currently in progress.

Specific capacitances measured for bare and heat-treated MnO_2 cryptomelane over extended voltammetric cycling are also illustrated in Figure 11. The bare sample exhibits a good electrochemical stability and an average capacitance value of 125 F · g^{-1}. Annealing the cryptomelane sample up to 400 °C engenders a slight decrease of the capacitance during cycling from 122 to 109 F · g^{-1}. On the other hand, annealing cryptomelane up to 600 °C improves both electrochemical performance and stability. This behavior could be caused either by the regeneration of mixed valence sites Mn^{4+}/Mn^{3+} (= MnO_2) in aqueous electrolytes or by the formation of a new 2D layered phase, i.e., $K_{0.51}Mn_{0.93}O_2$ contributing to the overall material capacitance.

CONCLUSIONS

The thermal behavior of various MnO_2 allotropes was investigated by in situ XRD and TGA measurements. The heat treatment of prepared MnO_2 compounds from 25 to 200 °C results in the removal of water molecules from their surfaces. This leads to significant morphological changes for most MnO_2 phases. In fact, the departure of H_2O from spinel, birnessite, Ni-todorokite, and OMS-5 lattices engenders a rapid crushing of their corresponding structures. However, the crystal structures of pyrolusite, ramsdellite, and cryptomelane are still stable up to 200 °C due to their low water content. Among all MnO_2 forms investigated here, only pyrolusite and cryptomelane conserved their structures when the temperature was increased up to 400 °C. For temperatures exceeding 400 °C, the whole MnO_2 set shows drastic structural modifications accompanied by the formation of numerous manganese oxide byproducts. For example, the 3D spinel configuration changed to 1D channels (1 × 1 and 1 × 2 tunnels) at 400 °C. This is attributed to the removal of lithium ions from the spinel vacancy sites. Moreover, the 1D cryptomelane structure was converted to

a 2D layer-one ($K_{0.51}Mn_{0.93}O_2$) at 600 °C due to the loss of 2 × 2 channel pillars. In the same way, the 1D Ni-todorokite compound was transformed to a 3D one ($NiMn_2O_4$) at 400 °C. This is explained by the release of a significant amount of H_2O molecules from the large 3 × 3 todorokite tunnels. When the temperature was increased up to 800 °C, Mn_3O_4 was obtained as a final product, independently of the manganese dioxide pristine form.

Electrochemical experiments showed that CV curves of MnO_2 cryptomelane-based electrodes are identical before and after heat treatments up to 400 and 600 °C, confirming cryptomelane as electrochemically stable upon heating. The long-term voltammetric cycling shows a suitable electrochemical stability for the bare and heat-treated cryptomelane. On the other hand, Mn_3O_4-based electrode presents the lowest specific capacitance in the series. However, the electrochemical performance of Mn_3O_4 may be considerably improved by successive cycling thanks to a progressive conversion to MnO_2.

Acknowledgment. The authors thank the Centre National de la Recherche Scientifique (CNRS) and the Agence Nationale de la Recherche (ANR) for financial support through the ABHYS project.

REFERENCES AND NOTES

(1) Fritsch, S.; Post, J. E.; Suib, S. L.; Navrotsky, A. *Chem. Mater.* **1998**, *10*, 474–479.
(2) Chabre, Y.; Pannetier, J. *Prog. Solid State Chem.* **1995**, *23*, 1–130.
(3) Shen, Y. F.; Zerger, R. P.; DeGuzman, R. N.; Suib, S. L.; McCurdy, L.; Potter, D. I.; O'Young, C. L. *Science* **1993**, *260*, 511–515.
(4) Feng, Q.; Kanoh, H.; Ooi, K. *J. Mater. Chem.* **1999**, *9*, 319–333.
(5) Kang, K. S.; Meng, Y. S.; Bréger, J.; Grey, C. P.; Ceder, G. *Science* **2006**, *311*, 977–980.
(6) Brock, S. L.; Duan, N. G.; Tian, Z. R.; Giraldo, O.; Zhou, H.; Suib, S. L. *Chem. Mater.* **1998**, *10*, 2619–2628.
(7) Toupin, M.; Brousse, T.; Bélanger, D. *Chem. Mater.* **2004**, *16*, 3184–3190.
(8) DeGuzman, R. N.; Shen, Y.-F.; Neth, E. D.; Suib, S. L.; O'Young, C.-L.; Levine, S.; Newsam, J. M. *Chem. Mater.* **1994**, *6*, 815–821.
(9) Feng, Q. *J. Mater. Sci. Lett.* **2003**, *22*, 999–1001.
(10) Cheney, M. A.; Bhowmik, P. K.; Qian, S.; Joo, S. W.; Hou, W.; Okoh, J. M. *J. Nanomater.*, ID 940462 2009 (DOI: 10.1155/2009 940462).
(11) Bowden, W.; Bofinger, T.; Zhang, F.; Iltchev, N.; Sirotina, R.; Paik, Y.; Chen, H.; Grey, C.; Hackney, S. *J. Power Sources* **2007**, *165*, 609–615.
(12) Prieto, O.; Del Arco, M.; Rives, V. *Thermochim. Acta* **2003**, *401*, 95–109.
(13) Ching, S.; Roark, S.; Duan, J. L.; Suib, S. L. *Chem. Mater.* **1997**, *9*, 750–754.
(14) Feng, Q.; Kanoh, H.; Miyai, Y.; Ooi, K. *Chem. Mater.* **1995**, *7*, 1226–1232.
(15) Ghodbane, O.; Pascal, J. L.; Fravier, F. *ACS Appl. Mater. Interfaces* **2009**, *1*, 1130–1132.
(16) Lv, D.; Huang, X.; Yue, H.; Yang, Y. *J. Electrochem. Soc.* **2009**, *156*, A911–A916.
(17) Zaki, M. I.; Hasan, M. A.; Pasupulety, L.; Kumari, K. *Thermochim. Acta* **1997**, *303*, 171–181.
(18) Nohman, A. K. H.; Zaki, M. I.; Mansour, S. A. A.; Fahim, R. B.; Kappenstein, C. *Thermochim. Acta* **1992**, *210*, 103–121.
(19) Rao, C. N. R.; Cheetham, A. K.; Mahesh, R. *Chem. Mater.* **1996**, *8*, 2421–2432.
(20) Hill, L. I.; Verbaere, A. *J. Solid State Chem.* **2004**, *177*, 4706–4723.
(21) Al-Sagheer, F. A.; Zaki, M. I. *Microporous Mesoporous Mater.* **2004**, *67*, 43–52.
(22) Liu, B.; Thomas, P. S.; Ray, A. S.; Williams, R. P.; Donne, S. W. *J. Therm. Anal. Calorim.* **2007**, *88*, 177–180.
(23) Paik, Y.; Bowden, W.; Richards, T.; Grey, C. P. *J. Electrochem. Soc.* **2005**, *152*, A1539–A1547.
(24) Ching, S.; Petrovay, D. J.; Jorgensen, M. L.; Suib, S. L. *Inorg. Chem.* **1997**, *36*, 883–890.
(25) Delmas, C.; Fouassier, C. *Z. Anorg. Allg. Chem.* **1976**, *420*, 184–192.
(26) Devaraj, S.; Munichandraiah, N. *J. Phys. Chem. C* **2008**, *112* (11), 4406–4418.
(27) Jeong, Y. U.; Manthiram, A. *J. Electrochem. Soc.* **2002**, *149*, A1419–A1422.
(28) Athouël, L.; Moser, F.; Dugas, R.; Crosnier, O.; Bélanger, D.; Brousse, T. *J. Phys. Chem. C* **2008**, *112*, 7270–7278.
(29) Yuan, J.; Liu, Z. -H.; Qiao, S.; Ma, X.; Xu, N. *J. Power Sources* **2009**, *189*, 1278–1283.
(30) Gonzalez, C.; Gutierrez, J. L.; Gonzalez-Verlasco, J. R.; Cid, A.; Arranz, A.; Arranz, J. F. *J. Therm. Anal.* **1996**, *47*, 93–102.
(31) Gaillot, A.-C.; Lanson, B.; Drits, V. A. *Chem. Mater.* **2005**, *17*, 2959–2975.
(32) Thackeray, M. M. *Prog. Solid State Chem.* **1997**, *25*, 1–71.
(33) De Wolff, P. M. *Acta Crystallogr.* **1959**, *12*, 341–345.
(34) Fritsch, S.; Post, J. E.; Suib, S. L.; Navrotsky, A. *Chem. Mater.* **1998**, *10*, 474–479.
(35) Nagao, M.; Pitteloud, C.; Kamiyama, T.; Otomo, T.; Itoh, K.; Fukunaga, T.; Kanno, R. *J. Electrochem. Soc.* **2005**, *152*, E230–E237.
(36) Valente, J. S.; Frías, D.; Navarro, P.; Montes, M.; Delgado, J. J.; Fregoso-Israel, E.; Torres-García, E. *Appl. Surf. Sci.* **2008**, *254*, 3006–3013.
(37) Hattori, H. *Chem. Rev.* **1995**, *95*, 537–558.
(38) Post, J. E.; Heaney, P. J.; Hanson, J. *Am. Mineral.* **2003**, *88*, 142–150.
(39) Bodak, O.; Akselrud, L.; Demchenko, P.; Kotur, B.; Mrooz, O.; Hadzaman, I.; Shpotyuk, O. *J. Alloys Compd.* **2002**, *347*, 14–23.
(40) Ching, S.; Krukowska, K. S.; Suib, S. L. *Inorg. Chim. Acta* **1999**, *294*, 123–132.
(41) Kumagai, N.; Komaba, S.; Abe, K.; Yashiro, H. *J. Power Sources* **2005**, *146*, 310–314.
(42) Bordet-Le Guenne, L.; Deniard, P.; Biensan, P.; Siret, C.; Brec, R. *J. Mater. Chem.* **2000**, *10*, 2201–2206.
(43) Komaba, S.; Ogata, A.; Nakagawa, D. *ITE Lett.* **2007**, *8*, 400–404.
(44) Messaoudi, B.; Joiret, S.; Keddam, M.; Takenouti, H. *Electrochim. Acta* **2001**, *46*, 2487–2498.
(45) Broughton, J. N.; Brett, M. J. *Electrochim. Acta* **2004**, *49*, 4439–4446.
(46) Djurfors, B.; Broughton, J. N.; Brett, M. J.; Ivey, D. G. *J. Electrochem. Soc.* **2006**, *153*, A64–A68.

AM100669K